Realization of geometric Landau-Zener-Stückelberg interferometry

Junhua Zhang, Jingning Zhang, Xiang Zhang, and Kihwan Kim[*]
Center for Quantum Information, Institute for Interdisciplinary Information Sciences, Tsinghua University, Beijing 100084, People's Republic of China

(Received 9 January 2013; revised manuscript received 22 August 2013; published 10 January 2014)

We report an experimental realization of the geometric Landau-Zener-Stückelberg (LZS) interferometry proposed by Gasparinetti *et al*. [Phys. Rev. Lett. **107**, 207002 (2011)] in a single-trapped-ion system. Unlike those in a conventional LZS interferometer, the interference fringes of our geometric interferometer originate solely from a geometric phase. We also observe the robustness of the interference contrast against noise or fluctuations in the experimental parameters. Our scheme can be applied to other complex systems subject to relatively large errors in system control.

DOI: 10.1103/PhysRevA.89.013608 PACS number(s): 03.75.Dg, 03.65.Vf, 03.65.Yz, 03.75.Lm

I. INTRODUCTION

The Landau-Zener (LZ) transition or Landau-Zener-Stückelberg (LZS) interferometry together with Rabi oscillation have been widely used to coherently control quantum systems, including atomic or optical systems [1–3], quantum dots [4,5], superconducting qubits [6,7], nitrogen-vacancy-(NV-) center systems [8], and spin transistors [9]. Related to the Rabi operation, composite pulses associated with dynamical decoupling [10–13] or adiabatic manipulation with geometric phases [14–16] have been extensively studied to reach error rates below the fault-tolerant level with reasonable limitations of control in feasible physical systems.

Generally, a quantum system subjected to adiabatic driving acquires a geometric phase (or Berry phase) as well as a dynamic phase. Unlike the dynamic phase, the geometric phase depends solely on the trajectory of the parameters in the Hamiltonian, and thus is stable against certain types of fluctuations; this has been experimentally observed in various systems [17–20]. Composite-pulse schemes also have a geometric phase interpretation in nonadiabatic regimes [21,22]. However, the geometric phase and robust control in the context of LZ interferometry have' not yet been experimentally investigated and demonstrated [23,24].

Here, we report an experimental realization of LZS interferometry controlled exclusively by the geometric phase; it is inspired by the proposal of Ref. [23] in a single-trapped-ion system, which is capable of simulating other quantum two-level (qubit) systems. Although the original proposal is specifically for a superconducting system, we apply the scheme to a trapped-ion system and observe the robustness of the geometric phase against very great operational errors in *all* possible control parameters by artificially introducing noise into the system. Our demonstration of strong immunity sheds light on the possibility of examining the geometric phase in more complex systems which might be subject to large fluctuations in control parameters. Furthermore, our realization contains the basic procedure for adiabatic quantum simulation and can be extended to investigate and harness the geometric phase in many-body systems for quantum information processing [15,25].

II. TRAPPED-ION SYSTEM FOR GEOMETRIC LZS INTERFEROMETRY

The geometric LZS interferometry of a qubit system can be described by the following Hamiltonian:

$$H_{\mathrm{GLZ}}(t) = \frac{\hbar}{2}\boldsymbol{\sigma}\cdot\mathbf{B}_{\mathrm{eff}}(t), \tag{1}$$

where $\boldsymbol{\sigma} = (\sigma_x, \sigma_y, \sigma_z)$ is the vector of Pauli matrices and the effective magnetic field $\mathbf{B}_{\mathrm{eff}} \equiv (B_x, B_y, B_z) = (\Omega\cos\varphi, \Omega\sin\varphi, \Delta)$. Here Δ is the energy splitting of the qubit system at the avoided crossing and Ω is the driving strength of the system. We denote $\hbar = 1$ for convenience.

We realize the geometric LZS interferometer in a single $^{171}\mathrm{Yb}^{+}$ ion as a model qubit. The single $^{171}\mathrm{Yb}^{+}$ ion is trapped in a four-rod radio -requency trap [26,27] as shown in Fig. 1(a). We map the two internal levels of the $^{171}\mathrm{Yb}^{+}$ ion in the $S_{1/2}$ ground-state manifold to the qubit states; this is represented by $|F = 1, m_F = 0\rangle \equiv |\uparrow\rangle$ and $|F = 0, m_F = 0\rangle \equiv |\downarrow\rangle$. The energy splitting of the two levels results from the hyperfine interaction, and the transition frequency between the $|\uparrow\rangle$ state and the $|\downarrow\rangle$ state is $\omega_{\mathrm{hf}} = (2\pi)12\,642.821$ MHz. Coherent driving is implemented by a microwave with a frequency detuned by $\Delta(t) = \omega_{\mathrm{hf}} - \omega_{\mathrm{M}}(t)$ and strength Ω as depicted in Fig. 1(b). We control Δ and Ω by mixing the microwave signal with the output of an arbitrary-wave-form generator (AWG) of 1 GSamples/s, which is significantly high to ignore the sampling effect compared to the typical operation time, a few hundred microseconds, as shown in Fig. 1(d). By going to the interaction picture defined by $H_{\mathrm{M}} = \frac{\sigma_z}{2}\omega_{\mathrm{M}}(t)$, we obtain the geometric LZS Hamiltonian, H_{GLZ} (1), where φ is the phase of the microwave source. In the experiment, we first apply Doppler cooling and initialize the state to the $|\downarrow\rangle$ state by the standard optical pumping technique with 99.1% efficiency [26,27]. At the end of the experimental sequence, we measure the population of the $|\uparrow\rangle$ state by applying a fluorescent detection scheme [26,27], and the typical photon distribution for the difference states is shown in Fig. 1(c).

III. EXPERIMENTAL PROCEDURE FOR GEOMETRIC LZS INTERFEROMETRY

The whole procedure for the geometric LZS interferometry is shown in Fig. 2(a) as sequences of experimental

[*]kimkihwan@mail.tsinghua.edu.cn

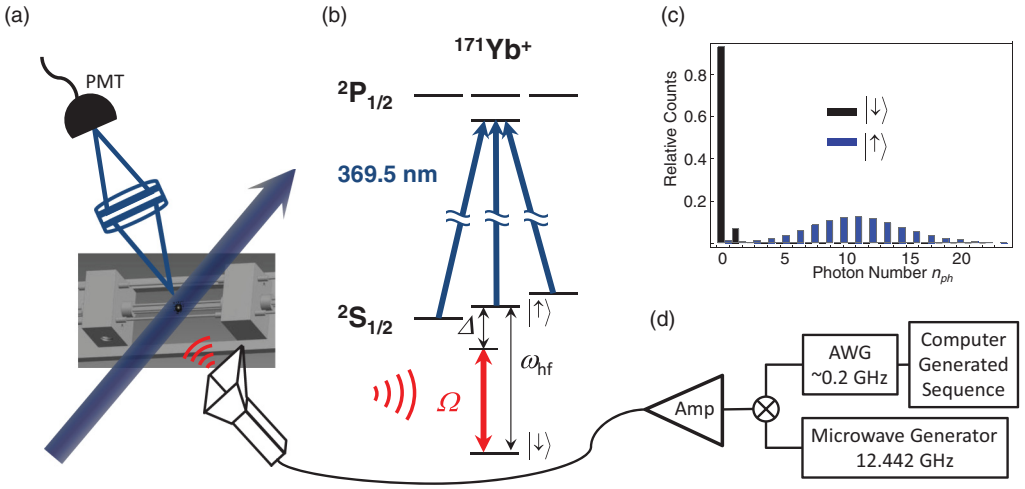

FIG. 1. (Color online) Experimental setup for the realization of geometric LZS interferometry. (a) The schematic diagram of a standard four-rod rf trap, detection system, and microwave operation system. (b) The energy-level diagram of the $^{171}Yb^{+}$ ion with the detection laser beam and microwave nearly resonant with the qubit system for geometric LZS interferometry. (c) Histograms of detected photons after the ion is prepared in each of the two qubit states. (d) Experimental apparatus for the control of the amplitude and the frequency of the applied microwave.

controls of Δ and Ω. The interferometer basically consists of two successive LZ transitions, which are equivalent to the beam splitters of a Mach-Zehnder interferometer, where the interference fringes are solely determined by the geometric phase. The dynamical phases accumulated between the LZ transitions are completely removed by an adiabatic spin-echo scheme [28,29]. In detail, the sequences are decomposed to five main procedures and the adiabatic spin echo: (1) $[t_1,t_2]$, adiabatic preparation of the instantaneous ground state of the initial Hamiltonian; (2) $[t_2,t_3]$, LZ transition; (3a),(3b) $[t_3,t_4]$ and $[t_6,t_7]$ adiabatic evolutions to accumulate a geometric phase; (4) $[t_7,t_8]$, LZ transition; (5) $[t_8,t_9]$ adiabatic rotation to transfer the final state to the measurement basis σ_z; and (S1),(S2) $[t_4,t_6]$, spin-echo sequence to eliminate the dynamic phase and the Stokes phase. The interference pattern of the geometric phase is observed by measuring the population of the upper eigenstate in the measurement basis. Figures 2(b)–2(e) show the trajectories of $\mathbf{B}_{\rm eff}$ in the (B_x,B_y,B_z) space and Figs. 2(f)–2(i) show the evolutions of the qubit state in E-$\mathbf{B}_{\rm eff}^{\perp}$ space with changes of the parameters

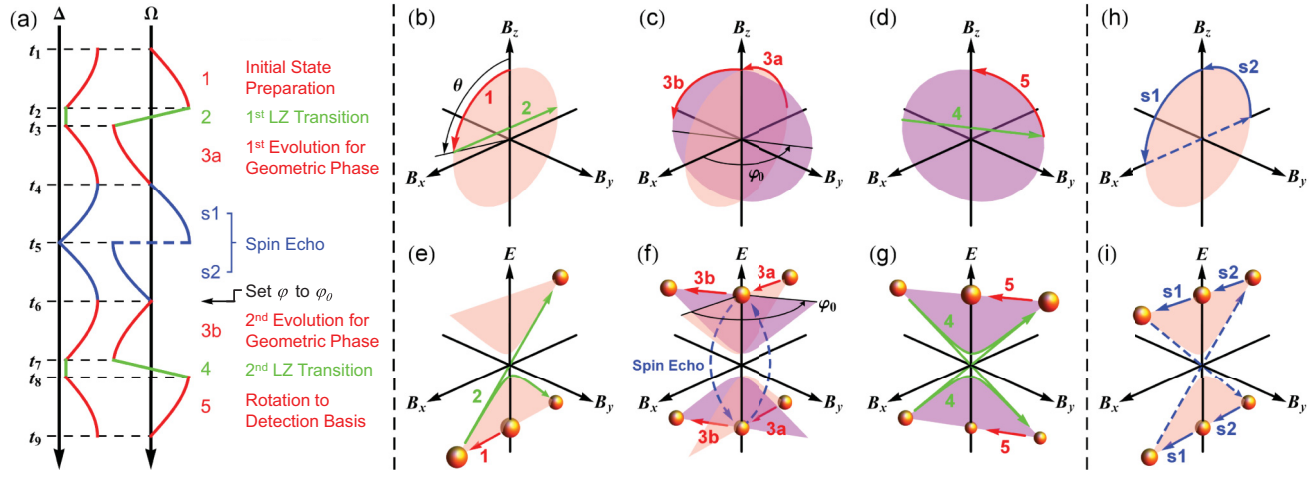

FIG. 2. (Color online) (a) The control sequences of Δ and Ω in $\mathbf{B}_{\rm eff}=(\Omega\cos\varphi,\Omega\sin\varphi,\Delta)$ for the realization of geometric LZS interferometry. The sequences are composed of (1) adiabatic state preparation $[t_1,t_2]$, (2) the first LZ transition $[t_2,t_3]$, (3a), (3b) adiabatic evolutions for acquiring the geometric phase $[t_3,t_4]$ and $[t_6,t_7]$, (4) the second LZ transition $[t_7,t_8]$, (5) final rotation to the measurement basis $[t_8,t_9]$ and adiabatic spin-echo sequence $[t_4,t_6]$. At $t=t_6$, we change the phase of ϕ from 0 to ϕ_0. Adiabatic procedures are noted in red [(1), (3a), (3b), and (5)] except for the spin-echo sequences. The colors and numbers used in (a) remain consistent in all the other figures. (b)–(d) The trajectories of $\mathbf{B}_{\rm eff}$ during the operation in (B_x,B_y,B_z) space. (e)–(g) The description of geometric LZS interferometry in E-$\mathbf{B}_{\rm eff}^{\perp}$ space, where the hyperbolic curves indicate the adiabatic eigenenergies. In contrast to the standard energy diagram for the LZ transition, the geometric LZS interferometer should be described in three-diemsnional (3D) space due to the phase information. The volume of the orange spheres corresponds to the population of the adiabatic eigenstates. (h) The trajectories of $\mathbf{B}_{\rm eff}$ for the adiabatic spin-echo sequences. (i) The description of the spin-echo sequences in E-$\mathbf{B}_{\rm eff}^{\perp}$ space.

in the Hamiltonian, where the hyperbolic curves indicate the adiabatic eigenenergies $E_{\pm} = \pm\sqrt{\Delta_0^2 + \Omega^2}$.

For the implementation of the geometric LZS interferometer, the adiabatic evolution, where a parameter of a Hamiltonian slowly changes and the system follows the ground state of the instantaneous Hamiltonian, plays a crucial role as the main method for state preparation, state detection, state inversion, and geometric phase generation. Therefore, we carefully investigate the validity of adiabaticity in our experimental realization. We also perform an experimental study of the LZ transition, where the separation probability between two instantaneous energy eigenstates is controlled by the sweeping rate in the vicinity of the avoided crossing. Based on the experimental confirmation of the validity of adiabatic evolution and of the ability to control the LZ transition, we perform geometric LZS interferometry.

A. Adiabatic evolution

Adiabatic evolution is used for the sequences of (1), (3a), (3b), and (5) as well as (S1) and (S2). We apply adiabatic evolution to rotate the $\mathbf{B}_{\text{eff}}$ field about an axis on the x-y plane by changing the amplitude Ω and the detuning Δ of the microwave in the following manner:

$$\Omega(t) = |\mathbf{B}_{\text{eff}}| \sin\theta(t), \quad \Delta(t) = |\mathbf{B}_{\text{eff}}| \cos\theta(t), \qquad (2)$$

where $|\mathbf{B}_{\text{eff}}|$ is the magnitude of the effective magnetic field, and θ is linearly increasing in time, $\theta(t) = (\theta_f / T_a)t$. We chose the change rate $\theta_f / T_a = \pi/(200\ \mu\text{s})$ for $|\mathbf{B}_{\text{eff}}| = (2\pi)50$ kHz, which is small enough to satisfy adiabaticity. With this rate, the initial ground state $|\downarrow\rangle$ evolves as the blue curve shown on the Bloch sphere of Fig. 3(a), where $\varphi = 0$. The time dependency of the populations of the $|\uparrow\rangle$ state is measured and compared to results of numerical calculations [Fig. 3(b)]. The difference in population between the experimental data and the ideal adiabatic evolution is no more than 5.5%.

B. LZ transition

The LZ transition is used for the sequences of (2) and (4). The LZ transition is investiaged including time-resolved measurement of the tunneling dynamics, similarly to the demonstration with cold atoms [30]. LZ tunneling occurs in the vicinity of the avoided crossing and in the long-time limit, the probability transferred to the upper energy eigenstate of the adiabatic basis after the transition is characterized by

$$P_{\text{LZ}} = \exp\left(-\frac{\pi\Delta_0^2}{2|v|}\right), \qquad (3)$$

where $v = \frac{d\Omega}{dt}|_{\Omega=0}$. In the adiabatic impulse approach, the transition in the adiabatic basis $\{|\psi_-\rangle, |\psi_+\rangle\}$ is described by the evolution matrix $U_{\text{LZ}} = U_a N U_b$ with

$$N = \begin{pmatrix} e^{-i\varphi_s}\sqrt{1-P_{\text{LZ}}} & -\sqrt{P_{\text{LZ}}} \\ \sqrt{P_{\text{LZ}}} & e^{i\varphi_s}\sqrt{1-P_{\text{LZ}}} \end{pmatrix}, \qquad (4)$$

where φ_s is the Stokes phase [31] and $U_{a(b)} = \exp(i\xi_{a(b)}\sigma_z)$, where $\xi_{a(b)}$ is the dynamic phase accumulated after (or before) the LZ transition point.

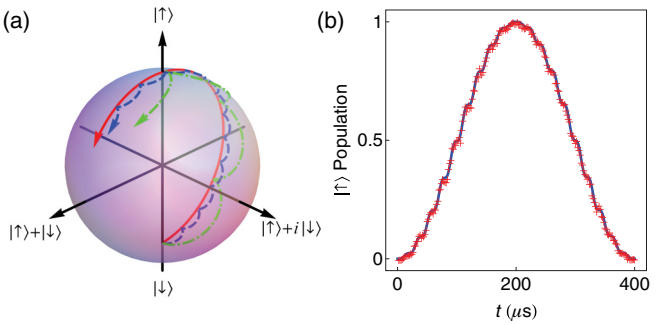

FIG. 3. (Color online) (a) The adiabatic evolution of the state. The traces of the system depending on the speeds of change in parameters are shown on the Bloch sphere in the case of $\varphi = 0$. The red curve is the trace of the perfect adiabatic evolution from the $|\downarrow\rangle$ state to the ground state of $H_{\text{GLZ}} = (\Delta/2)\sigma_z + (\Omega_i/2)\sigma_x$. We change Δ and Ω as shown in Eq. (2). The blue dashed and the green dash-dotted curves are the trajectories with speeds $\theta_f/T_a = \pi/(200\ \mu\text{s})$ and $\pi/(60\ \mu\text{s})$, respectively, with $|\mathbf{B}_{\text{eff}}| = (2\pi)50$ kHz. (b) The population of the $|\uparrow\rangle$ state. During adiabatic rotation, the rotation speed is $\pi/(200\ \mu\text{s})$, which is used thoughout the rest of the paper. The solid line shows the numerical estimation of the evolution in the $|\uparrow\rangle$ state population and the + symbols show the experimental data after averaging the measurements of 1500 trials, where the projection error of each point (0.012) is smaller than the size of the symbol. Note that we use the same conventions and perform the same number of trials for one data point throughout this paper.

Experimentally, we use the sequences (1), (2), and (5) of Fig. 2 to study the LZ transitions: *Sequence (1)*. We prepare the ground state of the Hamiltonian (1) with $\Omega_i = (2\pi)49.24$ kHz, $\Delta_0 = (2\pi)8.68$ kHz, and $\varphi = 0$ by adiabatically rotating the $|\downarrow\rangle$ state about the y axis. *Sequence (2)*. We change $\Omega(t) = (1 - 2\frac{t}{T})\Omega_i$ linearly in time. *Sequence (5)*. At time t, we adiabatically bring the state to that in the measurement basis $[|\psi_-(t)\rangle \rightarrow |\downarrow\rangle, |\psi_+(t)\rangle \rightarrow |\uparrow\rangle]$, which enables us to measure the population of the excited state $|\psi_+(t)\rangle$ by observing the probability of the $|\uparrow\rangle$ state, which is equivalent to the transition probability. The population of the $|\uparrow\rangle$ state after the transition versus the duration of the transition is plotted in Fig. 4(a), where the experimental results and the transition formula of Eq. (3) are in precise agreement. We also observe the transient dynamics and oscillatory behavior of LZ tunneling in the vicinity of the transition point with various speeds of change of Ω shown in Fig. 4(b), with improved quantitative agreement compared to Refs. [8,30]. Note that there is no fitting parameter in the theoretical expectations in Fig. 4, since the parameters are independently measured.

IV. GEOMETRIC LZS INTERFEROMETER

The total procedure for the geometric LZS interferometer is described in Fig. 2(a). The geometric phases are accumulated by adiabatic processes between two LZ transitions and the dynamical phases are canceled out by the adiabatic spin-echo sequences. In Fig. 2(a), the sequences (3a) and (3b) are for gaining the geometric phases and the sequences (S1) and (S2) are for executing the spin echo, swapping the $|\uparrow\rangle$ and the $|\downarrow\rangle$ eigenstates. The other sequences [sequences (1), (2), and (5)] are performed in the exact same way as in studying

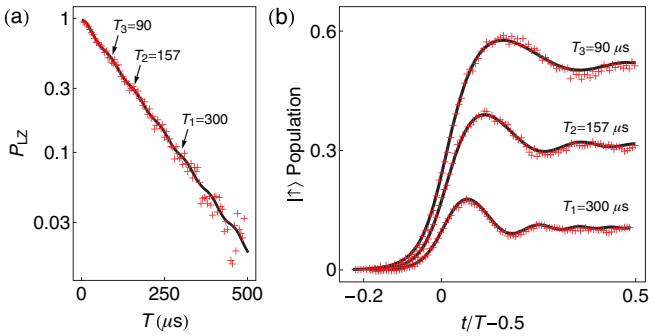

FIG. 4. (Color online) (a) LZ tunneling probability P_{LZ} as a function of the total sweeping time T of linear changes of Ω, where $\Delta_0 = (2\pi)8.68$ kHz and $\Omega_i = (2\pi)49.24$ kHz. (b) The LZ transition dynamics for three exemplary cases: the total durations T are 90 μs, 157 μs, and 300 μs, which provide tunneling probabilities of 0.5, 0.3, and 0.1 after the transitions. Oscillatory behaviors near the transition points [8,30] are clearly observed and precisely agree with the results of the numerical calculations.

the LZ transition as described above. Finally, we observe the interference fringes of the acquired geometric phases after the second LZ transition [sequence (4)] and adiabatic transfer of the population to the measurement basis [sequence (5)].

A. Geometric phase accumulation: Sequences (3a),(3b) and sequences (S1),(S2)

The accumulated geometric phase of each adiabatic eigenstate $\{|\psi_-\rangle, |\psi_+\rangle\}$ is given by

$$\gamma_\pm = i\int_{t_3}^{t_5} \langle\psi_\pm(t)|\frac{d}{dt}|\psi_\pm(t)\rangle dt. \quad (5)$$

The difference of geometric phase between the upper and lower eigenstates after the evolution is determined only by the rotation angle $\varphi_0 = (\gamma_+ - \gamma_-)$ of $\mathbf{B}_{\rm eff}$ as shown in Fig. 2(c), which is independent of the energy difference, the field amplitude change, or the duration of the interferometry. The dynamic phase is also acquired in the adiabatic processes. In order to erase the dynamical phase, we adiabatically invert only the state as depicted in Figs. 2(e) and 2(i) in the middle of the evolution [32]. The time evolution of the adiabatic spin-echo sequence (S1),(S2) is described as $U_{SE} = U_{a'}\sigma_x U_{b'}$, where $U_{a'(b')} = \exp(i\xi_{a'(b')}\sigma_z)$ is the dynamic phase accumulated after (or before) the spin-flip operation (σ_x). Due to the symmetry of the spin-echo sequences, the accumulated dynamic phases are canceled out and the time evolution operation U_G for these adiabatic stages is written as

$$U_G = \begin{pmatrix} e^{i\gamma_-} & 0 \\ 0 & e^{i\gamma_+} \end{pmatrix}. \quad (6)$$

B. Second LZ transition: Sequence (4)

The second LZ transition at $[t_7,t_8]$ in Fig. 2(a) is identical to the first LZ transition. The final state $|\psi(t_f)\rangle$ after the second LZ transition can be expressed in the following equation:

$$|\psi_f\rangle = U_{LZ}U_G U_{SE}U_{LZ}|\downarrow\rangle, \quad (7)$$

where the initial state is prepared as the instantaneous eigenstate with lower energy of the beginning Hamiltonian. Note that the Stokes phases occurring at the first and second LZ transitions are effectively canceled out because of the inversion of the state. Therefore, the final result is insensitive to the fluctuation of the Stokes phase as well as to the dynamic phase.

C. Rotation to measurement basis: Sequence (5)

At the final rotation $[t_8,t_9]$ in Fig. 2(a), we adiabatically transfer the population of the adiabatic basis to the measurement basis as discussed for the adiabatic process. Finally the population of the $|\uparrow\rangle$ state after the geometric LZS interferometry can be described by the simple formula

$$P_{|\uparrow\rangle} = P_{LZ}^2 + (1-P_{LZ})^2 - 2P_{LZ}(1-P_{LZ})\cos\varphi_0. \quad (8)$$

In the experiment, we set the transition probability $P_{LZ} = 1/2$, which simplifies (8) to $P_{|\uparrow\rangle} = \frac{1}{2}(1-\cos\varphi_0)$.

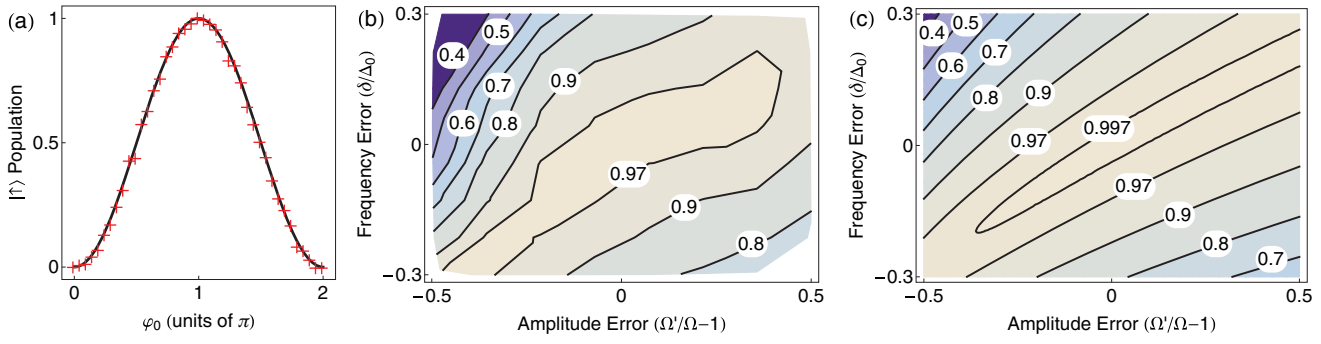

FIG. 5. (Color online) (a) The interference pattern of the geometric LZS interferometery. The final $|\uparrow\rangle$ state populations are determined only by the geometric phase of the rotation angle φ_0. The solid black line comes from the theoretical expectation Eq. (8) and the + symbols are experimental results (the average of 1500 trials). (b) The experimental data and (c) the theoretical estimation of the immunities in the interference contrast against the errors in the amplitude Ω and the frequency Δ of $\mathbf{B}_{\rm eff}$. The amplitude and the frequency errors are scaled by the ideal Ω and the minimum frequency gap Δ_0. The experimental figure (b) is constructed using fringe contrasts of 1139 random pairs of the amplitude Ω' and the frequency δ. At a given value of Ω' and δ, the reduction of the fringe contrast is inferred from the $|\uparrow\rangle$ state population $P(|\uparrow\rangle)$ obtained by 1500 repetitions of the experiment with $\varphi_0 = 0$. For several settings of Ω' and δ, we check that $1 - P(|\uparrow\rangle)$ at $\varphi_0 = 0$ is equivalent to the contrast within our detection errors (1.5%).

Figure 5(a) clearly shows that the populations of the $|\uparrow\rangle$ state at the end of the interferometry are solely determined by the geometric phase acquired during the adiabatic evolution, which is exactly the rotation angle ϕ_0. Figures 5(b) and 5(c) show the immunity of our interferometry to errors in the amplitude Ω and the frequency Δ which are both parameters in the effective field $\mathbf{B}_{\text{eff}}$. For the amplitude error scaled by the ideal strength, about $\pm 50\%$ changes reduce the contrast of the interference pattern by 20%, and for the frequency errors relative to the minimum gap Δ_0, $\pm 30\%$ offsets decrease the contrast by 20%. Here, we assume Ω' and $\Delta + \delta$ to be unchanged in a single experiment. In this case, the dynamic phase and Stokes phase are always canceled out, while the probability of the LZ transition changes between different experiments, which cause reduction of the interference contrast. We note that it has been shown that the geometric phase is robust against fast fluctuations of the control parameters, where the evolution time is longer than the typical noise correlation time [20].

V. CONCLUSION

In conclusion, we have realized a clear connection between the geometric phase and LZS interferometry and have observed the interference of the pure geometric phase. We have demonstrated the robustness of the interference against variations of all the parameters in $\mathbf{B}_{\text{eff}}$, which shows the possibility of observing such interference even in more complex systems, including superconducting qubit systems [23,32], quantum dot systems [33], NV-center diamond systems [8], etc. Within a trapped-ion system, our research makes possible an additional direction for performing multiqubit operations with the geometric phase in internal states [15,16], which can provide strong robustness and high fidelity of operation beyond the current methods that use the geometric phase in harmonic oscillators [34,35]. We also note that the experimental method used in the realization can be directly applied to adiabatic quantum computation.

ACKNOWLEDGMENTS

This work was supported in part by the National Basic Research Program of China Grants No. 2011CBA00300, No. 2011CBA00301, and No. 2011CBA00302, and the National Natural Science Foundation of China Grants No. 61073174, No. 61033001, and No. 61061130540. K.K. acknowledges support from the 1000 Plan Program for Young Talents.

[1] D. Bouwmeester, G. P. Karman, C. A. Schrama, and J. P. Woerdman, Phys. Rev. A **53**, 985 (1996).
[2] M. Mark, T. Kraemer, P. Waldburger, J. Herbig, C. Chin, H.-C. Nägerl, and R. Grimm, Phys. Rev. Lett. **99**, 113201 (2007).
[3] S. Kling, T. Salger, C. Grossert, and M. Weitz, Phys. Rev. Lett. **105**, 215301 (2010).
[4] J. R. Petta, H. Lu, and A. C. Gossard, Science **327**, 669 (2010).
[5] G. Cao, H.-O. Li, T. Tu, L. Wang, C. Zhou, M. Xiao, G.-C. Guo, H.-W. Jiang, and G.-P. Guo, Nat. Commun. **4**, 1401 (2013).
[6] S. Shevchenko, S. Ashhab, and F. Nori, Phys. Rep. **492**, 1 (2010).
[7] W. D. Oliver, Y. Yu, J. C. Lee, K. K. Berggren, L. S. Levitov, and T. P. Orlando, Science **310**, 1653 (2005).
[8] P. Huang, J. Zhou, F. Fang, X. Kong, X. Xu, C. Ju, and J. Du, Phys. Rev. X **1**, 011003 (2011).
[9] C. Betthausen1, T. Dollinger, H. Saarikoski, V. Kolkovsky, G. Karczewski, T. Wojtowicz, K. Richter, and D. Weiss, Science **337**, 324 (2012).
[10] L. M. K. Vandersypen and I. L. Chuang, Rev. Mod. Phys. **76**, 1037 (2004).
[11] K. R. Brown, A. W. Harrow, and I. L. Chuang, Phys. Rev. A **70**, 052318 (2004).
[12] M. J. Biercuk, H. Uys, A. P. Van Devender, N. Shiga, W. M. Itano, and J. J. Bollinger, Nature (London) **458**, 996 (2009).
[13] J. Du, X. Rong, N. Zhao, Y. Wang, J. Yang, and R. B. Liu, Nature (London) **461**, 1265 (2009).
[14] J. A. Jones, V. Vedral, A. Ekert, and G. Castagnoli, Nature (London) **403**, 869 (2000).
[15] L.-M. Duan, J. I. Cirac, and P. Zoller, Science **292**, 1695 (2001).
[16] O. Oreshkov, T. A. Brun, and D. A. Lidar, Phys. Rev. Lett. **102**, 070502 (2009).
[17] G. Falci, R. Fazio, G. M. Palma, J. Siewert, and V. Vedral, Nature (London) **407**, 355 (2000).
[18] A. Bohm, A. Mostafazadeh, H. Koizumi, Q. Niu, and J. Zwanziger, *The Geometric Phase in Quantum Systems* (Springer, New York, 2003).
[19] P. J. Leek, J. M. Fink, A. Blais, R. Bianchetti, M. Goppl, J. M. Gambetta, D. I. Schuster, L. Frunzio, R. J. Schoelkopf, and A. Wallraff, Science **318**, 1889 (2007).
[20] S. Filipp, J. Klepp, Y. Hasegawa, C. Plonka-Spehr, U. Schmidt, P. Geltenbort, and H. Rauch, Phys. Rev. Lett. **102**, 030404 (2009).
[21] Y. Ota and Y. Kondo, Phys. Rev. A **80**, 024302 (2009).
[22] T. Ichikawa, M. Bando, Y. Kondo, and M. Nakahara, Philos. Trans. R. Soc. A **370**, 4671 (2012).
[23] S. Gasparinetti, P. Solinas, and J. P. Pekola, Phys. Rev. Lett. **107**, 207002 (2011).
[24] M. D. Grace, J. M. Dominy, W. M. Witzel, and M. S. Carroll, Phys. Rev. A **85**, 052313 (2012).
[25] Y.-A. Chen, S. D. Huber, S. Trotzky, I. Bloch, and E. Altman, Nat. Phys. **7**, 61 (2011).
[26] S. Olmschenk, K. C. Younge, D. L. Moehring, D. N. Matsukevich, P. Maunz, and C. Monroe, Phys. Rev. A **76**, 052314 (2007).
[27] X. Zhang, M. Um, J. Zhang, S. An, Y. Wang, D.-L. Deng, C. Shen, L.-M. Duan, and K. Kim, Phys. Rev. Lett. **110**, 070401 (2013).
[28] M. V. Berry, J. Phys. A **42**, 365303 (2009).
[29] A. Ruschhaupt, X. Chen, D. Alonso, and J. G. Muga, New J. Phys. **14**, 093040 (2012).
[30] A. Zenesini, H. Lignier, G. Tayebirad, J. Radogostowicz, D. Ciampini, R. Mannella, S. Wimberger, O. Morsch, and E. Arimondo, Phys. Rev. Lett. **103**, 090403 (2009).
[31] Y. Kayanuma, Phys. Rev. A **55**, R2495 (1997).

[32] S. Berger, M. Pechal, S. Pugnetti, A. A. Abdumalikov, L. Steffen, A. Fedorov, A. Wallraff, and S. Filipp, Phys. Rev. B **85**, 220502(R) (2012).

[33] H. Wu, E. M. Gauger, R. E. George, Mikko, H. Riemann, N. V. Abrosimov, P. Becker, H.-J. Pohl, K. M. Itoh, M. L. W. Thewalt *et al*., Phys. Rev. A **87**, 032326 (2013).

[34] D. Leibfried, B. DeMarco, V. Meyer, D. Lucas, M. Barrett, J. Britton, W. M. Itano, B. Jelenkovic, C. Langer, T. Rosenband *et al*., Nature (London) **422**, 412 (2003).

[35] J. Benhelm, G. Kirchmair, C. F. Roos, and R. Blatt, Nat. Phys. **4**, 463 (2008).